Geometrical considerations of spaceborne SAR surveys

Marc Rodriguez-Cassola, German Aerospace Center, marc.rodriguez@dlr.de, Germany
Pau Prats-Iraola, German Aerospace Center, pau.prats@dlr.de, Germany
Rolf Scheiber, German Aerospace Center, rolf.scheiber@dlr.de, Germany
Alberto Moreira, German Aerospace Center, alberto.moreira@dlr.de, Germany

Abstract

In this paper, the conventional approximation of stationary locally range-dependent straight orbits for LEO spaceborne SAR surveys is analysed. This approximation breaks down in demanding scenarios, e.g., high-resolution, squinted, or bistatic SAR, which are likely to play an important role in future spaceborne SAR missions. The dependencies of the image formation parameters with respect to topography and squint are analysed. Further, an exemplary analysis of the expected variations along the orbit, i.e., azimuth variance, is presented. To complete the analysis, the impact of the intrapulse motion of the satellite in squinted geometries is considered. The understanding of the residual geometric components including the parameters having an impact on them is a first step to the development of efficient SAR image formation schemes for future challenging spaceborne SAR missions.

1 Introduction

The conventional approach for spaceborne SAR processing consists of a local substitution of the satellite orbit by a range-dependent straight trajectory [1, 2]. The range history of a given target will be then defined by its slant range and effective velocity, denoted as v_e, computed to match the hyperbolical model to the real geometry of the acquisition; thus, v_e depends on the satellite ephemerides and the target position. This model is capable of accommodating the variation of v_e with range, but deviations along the track occur. These deviations are basically due to topography, azimuth-varying squint angles, and the non-stationarity of the range migration along the track, i.e., the azimuth variance of the survey. The effects of these geometric errors introduce filter mismatch and may have an impact on the quality of the focussed SAR images in demanding scenarios like high-resolution, multi-swath, and bistatic SARs. Even if defocussing is kept at negligible levels, the focussed SAR images will suffer from phase and positioning errors [4].

2 Effective velocity and orbits

We analyse in this section the variation of the effective velocity due to the combined effect of the curvature of the orbits and the Earth rotation. We present the results using the effective velocity, v_e very illustrative for most of the community [3]. Moreover, as it has been shown in [4], this approach allows the derivation of analytical expressions as a function of the effective velocity, which might give a better feeling of the relevance of the discussed effects in many practical scenarios. In other cases where it might be required that the processing kernel accommodates non-hyperbolical range histories (e.g., bistatic surveys), the basic idea presented here would still apply, only the expressions would need to be derived as a function of other parameters, e.g., polynomial coefficients.

2.1 Dependence of the effective velocity with topography

This effect is relevant to high-resolution, squinted, and bistatic SAR surveys [5, 6]. Fig. 1 shows the typical scenario for the computation of the effective velocity considering topography. In the plot, the gray line shows the locus of targets at the same radar coordinates and different heights.

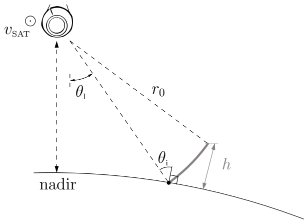

Figure 1: Cross-track geometry of a typical spaceborne SAR survey, with targets located at different heights.

The effective velocity of the targets varies with the topographic height. In typical LEO cases, this variation is linear, i.e.,

$$\frac{\partial v_\mathrm{e}}{\partial h} \approx f_v(\vec{p}_\mathrm{SAT}[n], r_0) \quad , \tag{1}$$

with f_v being the constant proportionality factor, depending on the orbit ephemerides, $\vec{p}_\mathrm{SAT}[n]$, around the azimuth coordinate of the target and on the slant range, noted r_0.

Eccentricity	0.001
Inclination	97.44 deg
Argument of perigee	90 deg
Ascending node	88.617 deg
Semimajor axis	6883.513 km

Table 1: Keplerian elements of the TerraSAR-X orbit.

Fig. 2 shows the variation of the effective velocity with the topographic height for a typical TerraSAR-X acquisition at 48 deg latitude, 35 deg incident angle. The Keplerian elements of the TerraSAR-X orbit listed in Table 1 were used for the computations. A total excursion of about 2 m/s over a range of 4 km in height is observed.

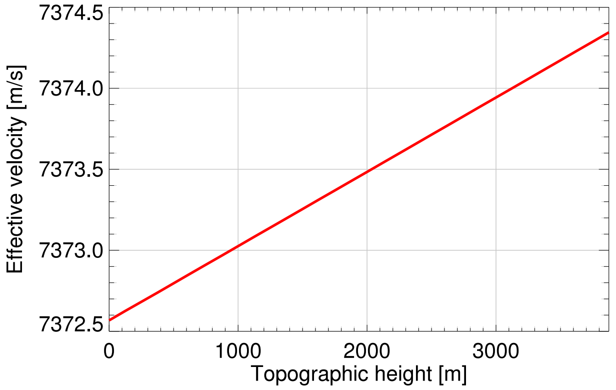

Figure 2: Effective velocity as a function of topography for a typical TerraSAR-X acquisition at 48 deg latitude, 35 deg incident angle.

The value of f_v increases with increasing orbit eccentricities, and increasing orbit heights. Fig. 3 shows the value of f_v in mHz for the TerraSAR-X case for different latitudes and incident angles. Note that the r_0 for the same incident angle vary with latitude due to the eccentricity of the orbit and the ellipsoidal form of the planet. However, the sensitivity to topography relaxes for higher incident angles, as it may be expected; concerning the variation along latitude, a factor six between the smallest and highest values can be observed. Note that the value of f_v for the analysed case in Fig. 2 is of about 0.5 mHz.

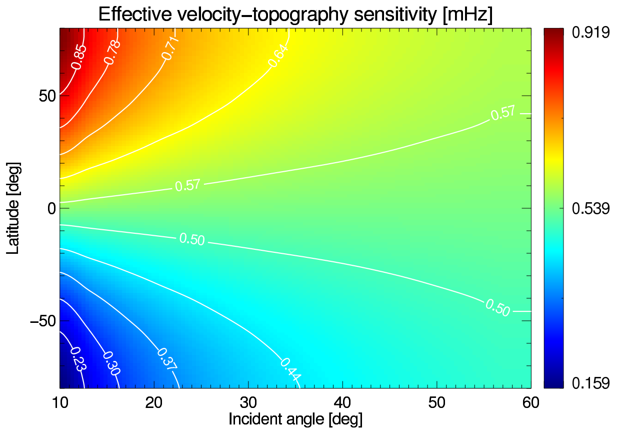

Figure 3: Values of f_v in mHz for a TerraSAR-X orbit as a function of the incident angle and the latitude.

2.2 Dependence of the effective velocity with squint

The dependence of the effective velocity with the squint is especially relevant in both bistatic SAR and SAR imaging modes with an azimuth-varying Doppler centroid, e.g., TOPS, ScanSAR, and spotlight. Fig. 4 shows the locus of targets at the same ranges and different positive squints

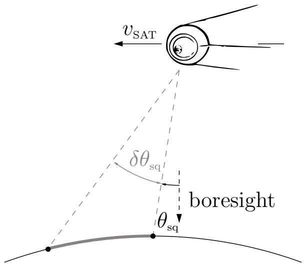

Figure 4: Cross-range geometry of a typical spaceborne SAR survey, with isorange targets observed with different squint angles.

As it may be expected, the dependence of the effective velocity on the squint angle of the acquisition shows a quadratic behaviour for typical LEO cases, i.e.,

$$\frac{\partial^2 v_\mathrm{e}}{\partial \theta_\mathrm{sq}^2} \approx k_\theta(\vec{p}_\mathrm{SAT}[n], r_0) \quad , \qquad (2)$$

where θ_sq is the squint angle and k_θ is the constant proportionality factor. For a typical TerraSAR-X acquisition at 48 deg latitude with 35 deg incident angle, the variation of v_e for a squint angle range between ± 10 deg is shown in Fig. 5. The total variation range is kept below 1.5 m/s.

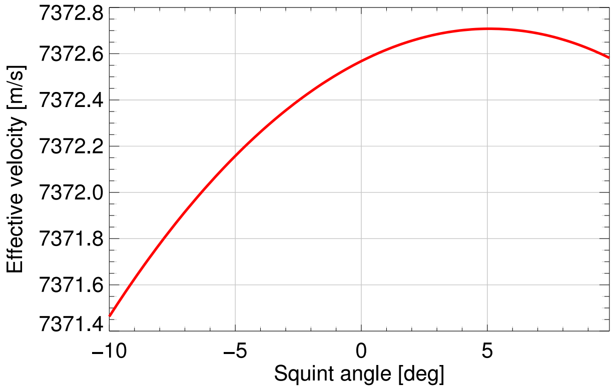

Figure 5: Effective velocity as a function of squint for a typical TerraSAR-X acquisition at 48 deg latitude, 35 deg incident angle.

2.3 Dependence of the effective velocity along the orbit: the azimuth variance

Even in the absence of topographic variations and antenna steerings, a mild change of v_e can be observed along the orbit. The azimuth variance refers to any other changes of the imaging geometry other than the scene (topography), and the observation angle (squint), e.g., change in the curvature of the orbit or changing bistatic baselines. The non-stationarity of the surveys has been a major issue in bistatic SAR due to the temporal variation of the baseline [6]. Azimuth variance has also been recognised as a principal problem in the development of high-resolution spaceborne SAR image formation algorithms [7, 8]. The azimuth variance seen in spaceborne SAR surveys is mainly caused by the rotation of the Earth, with a minor contribution due to the eccentricity and the inclination of the orbits. Fig. 6 shows the effective velocity for typical TerraSAR-X slant ranges (between 600 and 800 km) computed for different latitudes. The sweep range of the latitude is between ±75 deg. A variation of almost 70 m/s can be observed in the plot, with a linear dependence with slant range close to the Equator, and a quadratic behaviour when approaching the poles.

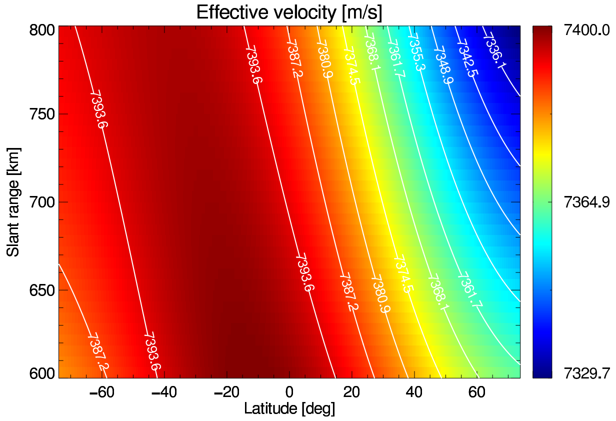

Figure 6: Effective velocity as a function of the latitude and the slant range for a TerraSAR-X like Keplerian acquisition.

If we now compute the derivative of the effective velocity along the track we get a better idea of the rate of change of v_e. For consistency, we denote the variation of v_e effective acceleration. The corresponding plot is shown in Fig. 7. A total variation of about 8.5 cm/s^2 can be observed in the plot.

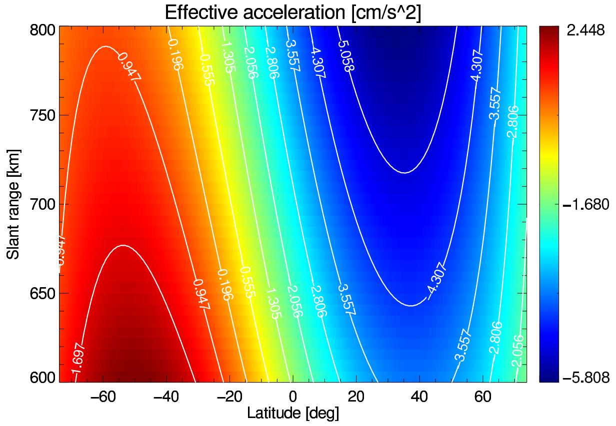

Figure 7: Effective acceleration as a function of the latitude and the slant range for a TerraSAR-X like Keplerian acquisition.

For slow changes of v_e, the velocity with which phase error and azimuth shifts vary due to the azimuth variance can be approximated by

$$\delta\dot{\phi} \approx \frac{4\pi \cdot r_0 \cdot a_\mathrm{e}}{\lambda \cdot v_\mathrm{e}} \cdot \left[\frac{\lambda^2 \cdot B_\mathrm{a}^2}{4 \cdot k \cdot v_\mathrm{e}^2} - \frac{\left(\frac{\lambda \cdot f_\mathrm{DC}}{2 \cdot v_\mathrm{e}}\right)^2}{\sqrt{1 - \left(\frac{\lambda \cdot f_\mathrm{DC}}{2 \cdot v_\mathrm{e}}\right)^2}} \right], \tag{3}$$

$$\delta\dot{t}_\mathrm{a} \approx \frac{-\lambda \cdot r_0 \cdot f_\mathrm{DC} \cdot a_\mathrm{e}}{v_\mathrm{e}^3}, \tag{4}$$

where r_0 is the slant range, a_e is the effective velocity, λ is the wavelength, v_e a reference effective velocity, B_a the azimuth processed bandwidth, f_DC the Doppler centroid, and k a constant roughly equal to 3 if no weighting is used during azimuth compression. Another interesting point in the analysis of the azimuth variance of a spaceborne SAR survey is the variation of the higher-than-2 order terms of the target range histories, which gives an idea of the need to update any wideband correction for long scenes. Fig. 8 shows the cubic coefficient of the actual range history for a TerraSAR-X like Keplerian orbit.

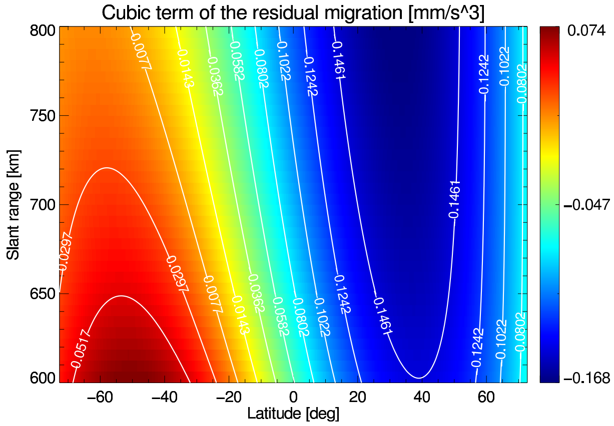

Figure 8: Cubic coefficient of the range history as a function of the latitude and the slant range for a TerraSAR-X like Keplerian acquisition.

3 The stop-and-go approximation in squinted geometries

A usual approximation in the SAR image formation literature has assumed the radar does not move during the transmission of the signal. Known as stop-and-go, this approximation has been thought particularly suitable for pulse SARs. The consequences of this approximation were analysed as early as in [2], i.e., a mismatch in the range compression (which may cause defocussing and a shift in range), and a mismatch in the azimuth compression, which may cause defocussing in azimuth and a range-dependent shift, as described in [8] and [9], respectively. First-order corrections of the stop-and-go approximation have been discussed in the framework of FMCW systems [10] and high-resolution pulse systems [8].

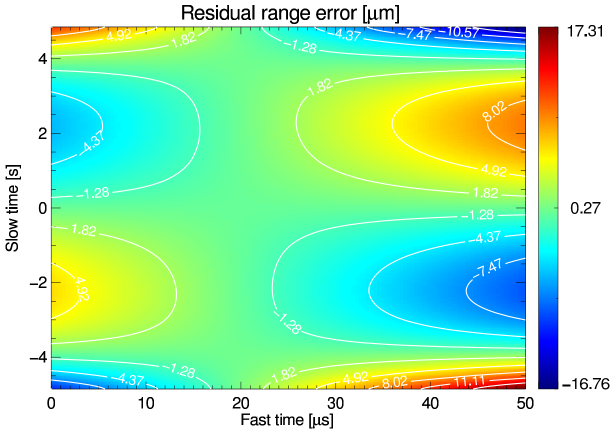

(a) 0 deg squint

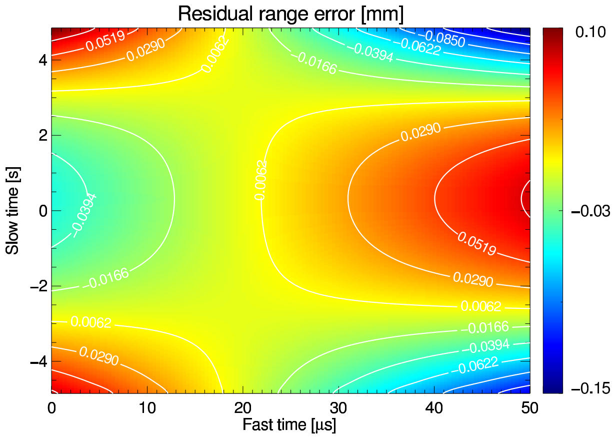

(b) 5 deg squint

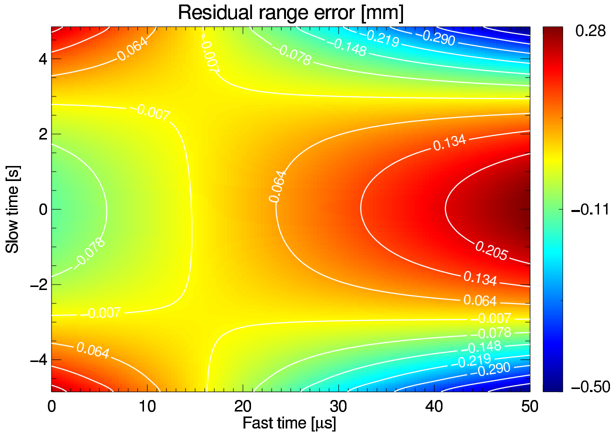

(c) 25 deg squint

Figure 9: Residual range history error after conventional SAR processing and further removal of a first-order compensation of the intrapulse motion of the satellite as a function of fast time and slow time for the reference orbit of Table 1 and three different squints from 0 deg (top) to 25 deg (bottom).

For the LEO orbit of Table 1, the residual range history caused by the intrapulse motion of the satellite fits the following model

$$\delta r(t_\mathrm{r}, t_\mathrm{a}) = p_k(\theta_\mathrm{sq}(t_\mathrm{a})) + q_m(\theta_\mathrm{sq}(t_\mathrm{a})) \cdot t_\mathrm{r}\ , \tag{5}$$

where t_r and t_a are the fast and slow times, θ_sq is the squint angle, and p_k and q_m are polynomials of order k and m, respectively. The order of k and m increases with the integration time; orders from 3 to 5 are enough to cover the span of usable squint angles in any case. Fig. 9 shows the residual range error with respect to the true range history after conventional SAR processing and the removal of a first-order error component as a function of the fast -pulse durations of up to 50 μs have been assumed- and slow times -integration times of up to 10 s- for three different squint angles, 0, 5, and 25 deg from top to bottom. As expected, for increasing squint angles the first-order compensation has increasing errors.

4 Conclusion

The paper has discussed the geometry of LEO spaceborne SAR, including an analysis of the dependences of the range history parameters with respect to topography, squint, azimuth variance, and the intrapulse motion of the satellite. The understanding of the residual geometric components and of the involved dependencies will surely play an essential role in the development of efficient SAR image formation schemes for future challenging spaceborne SAR missions including very high resolution, multiple swaths, and bistatic geometries.

References

[1] F. K. Li *et al.*, *Doppler parameter estimation for spaceborne synthetic aperture radars*, IEEE TGRS, jan. 1985.

[2] J. Curlander and R. McDonough, *Synthetic Aperture Radar: Systems and Signal Processing*, John Wiley, 1991.

[3] I. Cumming and F. Wong, *Digital Processing of Synthetic Aperture Radar Data. Algorithms and Implementation*, Artech House, 2005.

[4] M. Rodriguez-Cassola *et al.*, *Doppler-related distortions in TOPS SAR images*, accepted for publication in IEEE TGRS.

[5] T. Kempf *et al.*, *Depth-of-Focus Issues on Spaceborne Very High Resolution SAR*, Proc. IGARSS, Muenchen, 2012.

[6] M. Rodriguez-Cassola *et al.*, *Efficient time-domain image formation with precise topography accommodation for general bistatic SAR configurations*, IEEE TAES, oct. 2011.

[7] D. D'Aria *et al.*, *High-Resolution Spaceborne SAR Focusing by SVD-Stolt*, IEEE GRSL, aug. 2009.

[8] P. Prats *et al.*, *On the Processing of Very High Resolution Spaceborne SAR Data*, accepted for publication in IEEE TGRS.

[9] H. Breit *et al.*, *TerraSAR-X SAR Processing and Products*, IEEE TGRS, nov. 2010.

[10] A. Meta *et al.*, *Signal Processing for FMCW SAR* , IEEE TGRS, nov. 2007.

[11] P. Prats *et al.*, *TOPS Interferometry with TerraSAR-X*, IEEE TGRS, aug. 2012.